



Multi-layer configuration for the cathode electrode of polymer electrolyte fuel cell

Xuhui Feng, Yun Wang*

Renewable Energy Resources Lab (RERL) and National Fuel Cell Research Center, Department of Mechanical and Aerospace Engineering, The University of California, Irvine, Irvine, CA 92697-3975, USA

ARTICLE INFO

Article history:

Received 28 January 2010
Received in revised form 5 March 2010
Accepted 6 March 2010
Available online 16 March 2010

Keywords:

Polymer electrolyte fuel cell
Analysis
Electrode
Multi-layer
Reaction rate

ABSTRACT

This paper conducts a one-dimensional theoretical study on the electrochemical phenomenon in the dual-layer cathode electrode of polymer electrolyte fuel cells (PEFCs) with varying sub-layer thicknesses, and further extends the analysis to a triple-layer configuration. We obtain the explicit solution for a general dual-layer configuration with different layer thicknesses. Distributions of the key quantities such as the local reaction current and electrolyte overpotential are exhibited at different ratios of the ionic conductivities, electrochemical kinetics, and layer thicknesses. Based on the dual-layer approach, we further derive the explicit solutions for a triple-layer electrode. Sub-layer performances are plotted and compared. The results indicate that the layer adjacent to the electrolyte membrane may contribute a major part of the electrode faradic current production. The theoretical analysis presented in this paper can be applied to assist electrode development through complicated multi-layer configuration for cost-effective high performance electrodes.

© 2010 Elsevier Ltd. All rights reserved.

1. Introduction

Among the components of polymer electrolyte fuel cells (PEFCs), the cathode electrode is one of the most important parts [1,2]. The ORR (oxygen reduction reaction) in the cathode is sluggish comparing with the hydrogen oxidation reaction in the anode, contributing a major portion of the irreversible voltage loss. The ORR is highly heterogeneous across the cathode as indicated by our previous study [3,4]. The electrode structure can then be optimized for better cathode performance and cost reduction that still remains as a primary topic in PEFC development.

The mechanisms inside the cathode consist of diverse coupled chemical and physical processes, including electron/proton transport and heat/mass transfer. Modeling has been conducted by many groups to investigate the physical phenomena within the cathode. An early work was done by Eikerling and Kornyshev [5] to investigate cathode processes including the oxygen reduction, proton transport and oxygen diffusion. Analytical solutions were obtained, and these solutions helped to understand the impacts of the ORR, the geometrical and compositional parameters, and the oxygen partial pressure on fuel cell performance. You and Liu [6] assumed a pseudo-homogeneous electrode in their study. The overpotential, proton conductivity, catalyst layer porosity and surface area, were investigated and their impacts are evaluated. Boyer

et al. [7] presented simple mathematical expressions to optimize the fuel cell electrode structures, and those formula can be used to screen new materials for electrodes. Ticianelli et al. [8], Antoine et al. [9], Neyerlin et al. [10], and Das et al. [11] also conducted experimental or numerical studies on the electrode optimization or catalyst utilization, mostly for the single-layer configuration. Yoon et al. [12] proposed a multi-layer concept for improving the oxygen reduction in the cathode and prepared a dual-layer cathode using the spray-drying method. Its performance was evaluated in a single fuel cell by I - V curves. An agglomerate model was developed by Wang et al. [13] which considered the reaction kinetics, proton transport, and oxygen diffusion. The impacts of agglomerates on catalyst utilization and electrode efficiency were explored. Similar approach was also conducted by Jain et al. [14], which reformulated an agglomerate model to study the Pt minimization for a specified voltage. Another agglomerate model considers a 2D cathode [15,16]. Predictions showed that the charge transport is as important as oxygen diffusion in determining the overall electrode reaction rate [15] and suggested that further improvements in electrode performance at medium and high current density might be possible by reducing carbon loading and increasing the electrolyte content [16]. Wang et al. [17] considered the volume fraction of each constituent phase. They indicated that low humidity operation may benefit the performance under high current and a volume fraction of 0.4 and 0.26 for void and electrolyte phases, respectively, are the optimal composition for the considered electrode. A steady-state multi-layer agglomerate model was studied by Song et al. [18]. The model considers an elec-

* Corresponding author. Tel.: +1 949 824 6004; fax: +1 949 824 8585.
E-mail address: yunw@uci.edu (Y. Wang).

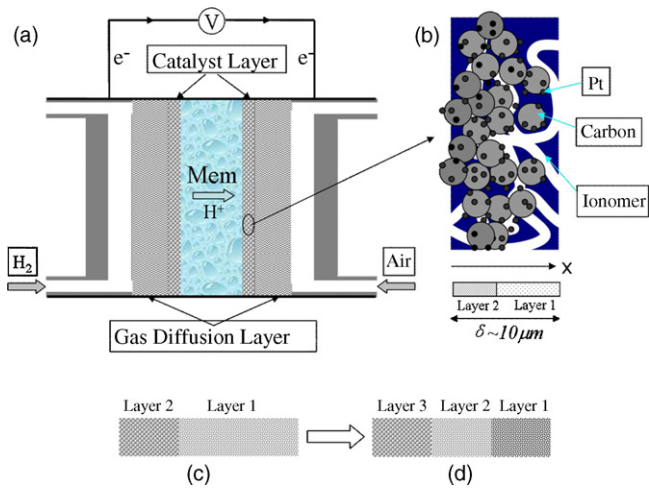


Fig. 1. Schematic of a PEMFC (a) and a general dual-layer catalyst layer (b), and connection between the dual-layer (c) and triple-layer (d) structures.

trode with several sub-layers. Numerical investigation showed that the performance of the catalyst layer may be considerably influenced by the properties of the sub-layer close to the membrane. Mukherjee and Wang [19] conducted a DNS (direct numerical simulation) on a dual-layer configuration with equal-thickness sub-layers. Our group obtained explicit solutions of the reaction rate profile for a single-layer [3] and a dual-layer [4] electrode. For the single-layer electrode, a considerable spatial variation of reaction rates was observed across the catalyst layer and a lumped parameter was identified to quantify the degree of this variation. The study on the dual-layer configuration considered an electrode consists of two equal-thickness sub-layers. Investigation was conducted on the impacts of the layer properties on electrode performance. Comprehensive reviews on electrode fabrication and optimization for fuel cells were recently provided by Refs. [20–23].

Following our dual-layer electrode analysis [4], this paper relaxes the restriction of equal thicknesses of the two sub-layers and develops explicit solutions for a general two-layer configuration and further a triple-layer one. Firstly, the thickness ratio of the two layers is included in the solution to investigate its impact on the overpotential profiles at varying ionic conductivity and effective exchange current density. Secondly, from the dual-layer solutions we derive the solution for a triple-layer electrode. Analysis is also conducted to investigate the reaction current within each layer and overall electrode performance. Further, this paper intends to use the triple-layer configuration as an example to introduce the multi-layer electrode concept. We choose to not include the discussion of four- or more-layer cases, whose explicit solutions are much more complex and longer. Note that the triple-layer solution takes a large space to express, which will be given in Appendix B.

2. Modeling and analytical solutions

2.1. General dual-layer configuration

A schematic configuration of a typical PEM fuel cell is displayed in Fig. 1, together with the magnified plot of a general dual-layer electrode. The left side of the electrode attaches the polymer electrolyte membrane, while the right connects to the diffusion media. There are three phases, in addition to the electrochemical catalyst, in the electrode that are necessary for its functions: (1) the void space for gaseous reactant transport; (2) ionomer content for protons transfer; and (3) carbon support for electronic current conduction. The dual-layer electrode is characterized by various sub-layers with specific properties assigned to each layer.

For convenience, we denote these sub-layers by Layers 1 and 2, respectively, as shown in Fig. 1. In these sub-layers, we consider the following parameters that may be different, the ionic conductivity, catalyst specific surface area, and exchange current density. These parameters are directly related to the electrolyte ionomer content ($\sigma_m^{eff} = \varepsilon_m^{1.5} \sigma_m$), electrode structure (e.g. reaction interface roughness), and catalyst Pt loading that are vital to the electrode fabrication. Note that the sub-layer porosity will likely be different with each other.

Among these sub-layers, we assume a uniform oxygen concentration C_{O_2} , temperature T , and electronic phase potential $\Phi^{(s)}$, which can be justified for PEM fuel cell electrodes following the same techniques in our previous analysis [4]. Note that Ref. [4] deals with a specific dual-layer electrode, i.e. with equal-thickness sub-layers. As long as the electrodes are thin and exhibit sufficient transport conductance, which is generally valid for PEM fuel cell, the assumptions will be valid for a general dual-layer configuration. For examples, varying porosities of sub-layers would not affect the assumption of a uniform oxygen concentration as long as they are in the typical range of fuel cell electrodes, i.e. >0.1 . The electronic conductivity of the catalyst layer, though may slightly vary from layer to layer, is typically much higher than the ionic one, therefore the ohmic loss due to the electronic resistance can be neglected across the two layers in the electrode. Also in the dual-layer configuration, the upper limit of temperature variation can be estimated through the formula of Eq. (11) in Ref. [3] as heat transfer is similar to species diffusion processes, except using the smaller thermal conductivity in the two layers. Even the smaller thermal conductivity decreases to 0.3 W/mK , the upper limit, which is reversely proportional to conductivity, is still small $\sim 0.1 \text{ K}$. Likewise, these assumptions can be further extended to the triple-layer case that will be discussed in the next section, as long as the sub-layer properties are in the range of a typical fuel cell electrode.

At steady state, the general equation of the electrolyte phase potential $\Phi^{(m)}$ s in the layer i (i is either 1 or 2) can be written as

$$\nabla \cdot [(\sigma_m^{eff})_i \nabla \Phi_i^{(m)}] + j_i = 0 \quad (1)$$

j_i is the transfer current density calculated from the Butler–Volmer equation,

$$j_i = -(aj_{0,T}^{ref,c})_i \left(\frac{C_{O_2}}{C_{O_2}^{ref}} \right) \exp \left(-\frac{\alpha_c F}{R_g T} \cdot (\Phi^{(s)} - \Phi_i^{(m)} - U_o) \right) \quad (2)$$

We define the thickness ratio of the two sub-layers as $r_{12}^\delta = \delta_1/\delta_2$. In the same manner, symbols r_{12}^{aj} and $r_{12}^{\sigma_m}$ denote the ratios of the effective exchange current densities and ionic conductivities, i.e. $r_{12}^{\sigma_m} = (\sigma_m^{eff})_1/(\sigma_m^{eff})_2$ and $r_{12}^{aj} = (aj_{0,T}^{ref,c})_1/(aj_{0,T}^{ref,c})_2$. Considering one-dimension (the through-plane or x direction), the boundary and interfacial conditions for Eq. (1) in the two layers are set as:

$$\Phi_1^{(m)} = \Phi_\delta^{(m)} \quad \text{and} \quad \frac{d}{dx} \Phi_1^{(m)} = 0 \quad \text{at} \quad x = \delta \quad (3)$$

$$\Phi_2^{(m)} = \Phi_1^{(m)} \quad \text{and} \quad \frac{d}{dx} \Phi_2^{(m)} = r_{12}^{\sigma_m} \frac{d}{dx} \Phi_1^{(m)} \quad \text{at} \quad x = \frac{1}{r_{12}^\delta + 1} \delta \quad (4)$$

Note that comparing with the case in the dual-layer configuration with equal-thickness sub-layers in Ref. [4], the interface changes to a more general location of $1/(r_{12}^\delta + 1)\delta$.

The explicit solution to the above problem is obtained as:

$$\begin{aligned} \Phi_1^{(m)} - \Phi_\delta^{(m)} &= \frac{R_g T}{\alpha_c F} \ln \left\{ \prod (\Delta U^{j_\delta, \bar{x}} + 1) \right\} \\ \Phi_2^{(m)} - \Phi_\delta^{(m)} &= \frac{R_g T}{\alpha_c F} \ln \left\{ \frac{\Psi^{II}(\Delta U^{j_\delta, \bar{x}}, r_{12}^{\sigma_m}, r_{12}^{aj}, r_{12}^\delta)}{[\Pi^{II}(\Delta U^{j_\delta, \bar{x}}, r_{12}^{\sigma_m}, r_{12}^{aj}, \bar{x}) + 1]} \right\} \end{aligned} \quad (5)$$

where

$$\begin{aligned} \Pi(\Delta U^{j\delta}, \bar{x}) &= \left[\tan \left(\pm \left[-\frac{\alpha_c F}{2R_g T} \Delta U^{j\delta} \right]^{1/2} \cdot (\bar{x} - 1) \right) \right]^2 \\ \Psi^{II} &= \Pi \left(\Delta U^{j\delta}, \frac{1}{r_{12}^\delta + 1} \right) (1 - r_{12}^{\sigma_m} \cdot r_{12}^{qj_0}) + 1 \\ \Upsilon^{II} &= \left[\tan \left(\sqrt{\frac{\alpha_c F \Delta U^{j\delta}}{2R_g T} \frac{r_{12}^{\sigma_m}}{r_{12}^{qj_0}}} \Psi^{II}(\Delta U^{j\delta}, r_{12}^{\sigma_m}, r_{12}^{qj_0}) \cdot \left(\bar{x} - \frac{1}{r_{12}^\delta + 1} \right) - \tan^{-1} \sqrt{\frac{\Pi \left(\Delta U^{j\delta}, \frac{1}{r_{12}^\delta + 1} \right)}{\Psi^{II}(\Delta U^{j\delta}, r_{12}^{\sigma_m}, r_{12}^{qj_0})} r_{12}^{\sigma_m} \cdot r_{12}^{qj_0}} \right) \right]^2 \end{aligned} \quad (6)$$

Note that the solution for the dual-layer electrode of equal-thickness sub-layers [4] is different with Eq. (6) only in the expression of functions Ψ^{II} and Υ^{II} . The variable $\Delta U^{j\delta}$ is defined based on the properties of Layer 1 [3]

$$\Delta U^{j\delta} = R_{\delta,1} j^\delta \quad \text{where } j^\delta = -j_\delta \delta, R_{\delta,1} = \frac{\delta}{(\sigma_m^{eff})_1} \quad \text{and } j_\delta = j(x = \delta) \quad (7)$$

Similarly, with the distribution of the electrolyte phase potential $\Phi^{(m)}$, the average current density within each layer can be calculated through the integral of the transfer current density,

$$\begin{aligned} \int_{\frac{1}{r_{12}^\delta + 1}}^1 |j(\bar{x})| d\bar{x} = I_1^{(2)} = -(\sigma_m^{eff})_1 \frac{d\Phi_1^{(m)}}{d\bar{x}} \Big|_{\bar{x}=\frac{1}{r_{12}^\delta + 1}} \\ \int_0^{\frac{1}{r_{12}^\delta + 1}} |j(\bar{x})| d\bar{x} = I_2^{(2)} = -(\sigma_m^{eff})_2 \frac{d\Phi_2^{(m)}}{d\bar{x}} \Big|_{\bar{x}=0} + (\sigma_m^{eff})_1 \frac{d\Phi_1^{(m)}}{d\bar{x}} \Big|_{\bar{x}=\frac{1}{r_{12}^\delta + 1}} \end{aligned} \quad (8)$$

where in $I_1^{(2)}$ and $I_2^{(2)}$ the superscript denotes the dual-layer configuration; the subscript the layer #. The average current density over the whole electrode can be expressed by:

$$\begin{aligned} I &= \sqrt{2 \frac{R_g T}{\alpha_c F} \frac{\Delta U^{j\delta}}{R_{\delta,1}^2}} \\ &\sqrt{r_{21}^{\sigma_m} \cdot r_{21}^{qj_0} \left[\Psi^{II} \cdot (\Upsilon^{II}(\Delta U^{j\delta}, 0) + 1) - \left(\Pi \left(\Delta U^{j\delta}, \frac{1}{r_{12}^\delta + 1} \right) + 1 \right) \right] + \Pi \left(\Delta U^{j\delta}, \frac{1}{r_{12}^\delta + 1} \right)} \end{aligned} \quad (9)$$

Note that the above equation build the direct relation between the average current density I and $\Delta U^{j\delta}$. $\Delta U^{j\delta}$ can be treated as a parameter that lumps several factors such as I , the ionic resistance, and sub-layer thickness ratio.

2.2. A triple-layer electrode

The general dual-layer result can be applied to obtain the explicit solution to the triple-layer electrode problem. For an instance,

Table 1
Physical parameters.

Quantity	Value
Exchange current density \times reaction surface area in Layer 1, $ai_0^{ref,c}$	10,000 A/m ³
Volume fraction/tortuosity of ionomer in electrodes in Layer 1, ε_m/τ_m	0.20/1.5
Transfer coefficient, α_c	1
Temperature, T	353.15
Pressure, P	2 atm
Activation energy for oxygen reduction reaction, E_a	73,269 J/mol

Fig. 2(a) shows a two-layer configuration. The Layer 1 in (a) can be further divided into two sub-layers, i.e. (b), which results in a triple-layer configuration. Therefore, the solution to a triple-layer configuration can be obtained by analyzing two dual-layer electrodes. Note that in order to apply the general dual-layer configuration solution, one needs to deal with non-homogeneous boundary conditions: following the same instance as above, the dual-layer, the Layers 2 and 3, will have a non-homogeneous boundary condition $(d/dx)\Phi_1^{(m)} \neq 0$, which requires special mathematical treatment. For simplicity, we only consider a triple-layer configuration with equal-thickness sub-layers. We denote the electrolyte phase potentials in the three layers $\Phi_1^{(m)}$, $\Phi_2^{(m)}$ and $\Phi_3^{(m)}$, respectively. The boundary and interfacial conditions to Eq. (1) become:

$$\begin{aligned} \Phi_1^{(m)} &= \Phi_\delta^{(m)} \quad \text{and} \quad \frac{d}{dx} \Phi_1^{(m)} = 0 \quad \text{at } x = \delta \\ \Phi_2^{(m)} &= \Phi_1^{(m)} \quad \text{and} \quad \frac{d}{dx} \Phi_2^{(m)} = r_{12}^{\sigma_m} \frac{d}{dx} \Phi_1^{(m)} \quad \text{at } x = \frac{2}{3} \delta \\ \Phi_3^{(m)} &= \Phi_2^{(m)} \quad \text{and} \quad \frac{d}{dx} \Phi_3^{(m)} = r_{23}^{\sigma_m} \frac{d}{dx} \Phi_2^{(m)} \quad \text{at } x = \frac{1}{3} \delta \end{aligned} \quad (10)$$

The explicit solution to this triple-layer problem can be found in Appendix B. Note that technically it is possible, though challenging, that we could find a solution to a general triple-layer case, i.e. with varying sub-layer thickness. However, it would not be necessary as no new physics could be explained (comparing with the equal-sub-layer thickness triple-layer configuration). In addition, the solution for this triple-layer configuration is already complicated and takes almost a page to express. The one to a general triple-layer configuration will be lengthy, therefore excluded in the present paper. The local transfer current density j in each sub-layer is then calculated by

$$\begin{aligned} \frac{j_1}{j_\delta} &= \Pi + 1, \quad \frac{j_2}{j_\delta} = \frac{1}{r_{12}^{qj_0}} \Psi^{II} \cdot (\Upsilon^{II} + 1), \quad \frac{j_3}{j_\delta} = \frac{1}{r_{13}^{qj_0}} \Psi^{III} \cdot (\Upsilon^{III} + 1) \end{aligned} \quad (11)$$

Following the approach similar to Eq. (8), the reaction currents generated in each sub-layer can be expressed as:

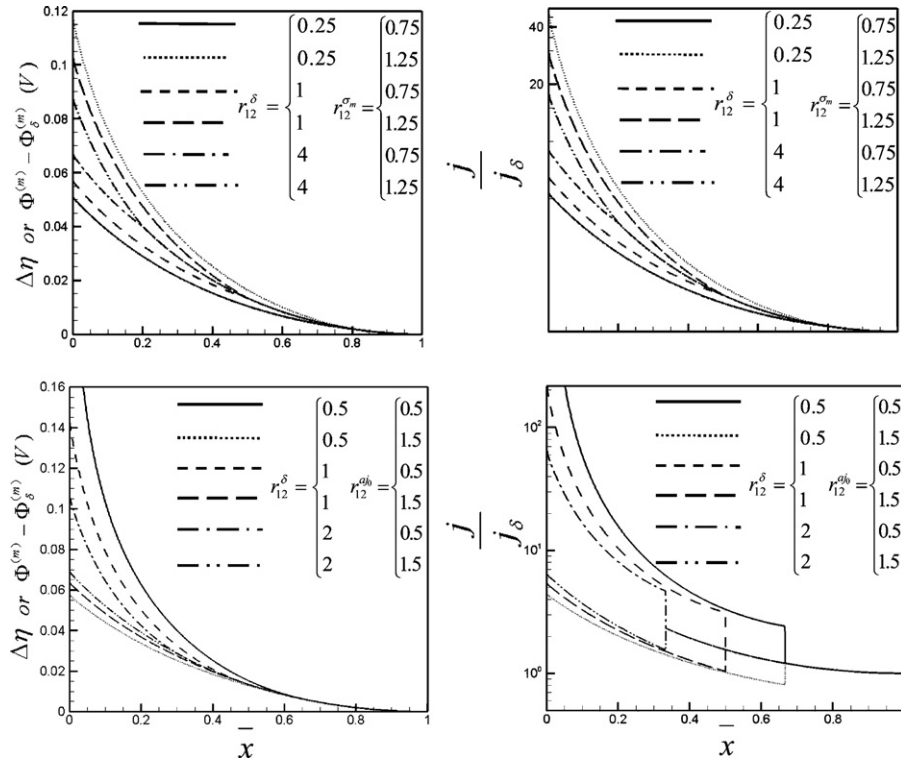


Fig. 2. Profiles of the overpotential variation $\Delta\eta$ or $\Phi^{(m)}(\bar{x}) - \Phi_{\delta}^{(m)}$ (left column) and the dimensionless reaction current j/j_{δ} (right column) in the electrode at varying ratios of sub-layer thicknesses r_{12}^{δ} s, ionic conductivities $r_{12}^{\sigma_m}$ s, and exchange current densities $r_{12}^{\sigma_0}$ s for $\Delta U_b = 0.1$ V.

$$\begin{aligned}
 \text{Layer 1 : } & \int_{2/3}^1 |j(\bar{x})| d\bar{x} = I_1^{(3)} = -(\sigma_m^{eff})_1 \left. \frac{d\Phi_1^{(m)}}{d\bar{x}} \right|_{\bar{x}=2/3} \\
 \text{Layer 2 : } & \int_{1/3}^{2/3} |j(\bar{x})| d\bar{x} = I_2^{(3)} = -(\sigma_m^{eff})_2 \left. \frac{d\Phi_2^{(m)}}{d\bar{x}} \right|_{\bar{x}=1/3} + (\sigma_m^{eff})_1 \left. \frac{d\Phi_1^{(m)}}{d\bar{x}} \right|_{\bar{x}=2/3} \\
 \text{Layer 3 : } & \int_0^{1/3} |j(\bar{x})| d\bar{x} = I_3^{(3)} = -(\sigma_m^{eff})_3 \left. \frac{d\Phi_3^{(m)}}{d\bar{x}} \right|_{\bar{x}=0} + (\sigma_m^{eff})_2 \left. \frac{d\Phi_2^{(m)}}{d\bar{x}} \right|_{\bar{x}=1/3}
 \end{aligned} \quad (12)$$

The current fluxes across the interfaces of $\bar{x} = \frac{2}{3}$, $\bar{x} = \frac{1}{3}$ and $\bar{x} = 0$ are expressed by

$$\begin{aligned}
 I_1^{(3)} &= -(\sigma_m^{eff})_1 \left. \frac{d\Phi_1^{(m)}}{d\bar{x}} \right|_{\bar{x}=2/3} = \sqrt{2 \frac{(\sigma_m^{eff})_1 R_g T}{\alpha_c F}} \sqrt{j_1(\bar{x}=1) - j_1(\bar{x}=\frac{2}{3})} \\
 I_1^{(3)} + I_2^{(3)} &= -(\sigma_m^{eff})_2 \left. \frac{d\Phi_2^{(m)}}{d\bar{x}} \right|_{\bar{x}=1/3} = \sqrt{2 \frac{(\sigma_m^{eff})_2 R_g T}{\alpha_c F}} \sqrt{\left(j_2(\bar{x}=\frac{2}{3}) - j_2(\bar{x}=\frac{1}{3}) \right) + r_{12}^{\sigma_m} \left(j_1(\bar{x}=1) - j_1(\bar{x}=\frac{2}{3}) \right)} \\
 I_1^{(3)} + I_2^{(3)} + I_3^{(3)} &= -(\sigma_m^{eff})_3 \left. \frac{d\Phi_3^{(m)}}{d\bar{x}} \right|_{\bar{x}=0} = \sqrt{2 \frac{(\sigma_m^{eff})_3 R_g T}{\alpha_c F}} \sqrt{\left(j_3(\bar{x}=\frac{1}{3}) - j_3(\bar{x}=0) \right) + r_{23}^{\sigma_m} \left(j_2(\bar{x}=\frac{2}{3}) - j_2(\bar{x}=\frac{1}{3}) \right) + r_{13}^{\sigma_m} \left(j_1(\bar{x}=1) - j_1(\bar{x}=\frac{2}{3}) \right)}
 \end{aligned} \quad (13)$$

Note that the above average current explicitly gives the contribution of each layer. The explicit solution can be directly applied in the electrode development using multi-layer configuration. Comparing with dual-layer configurations, a multi (>2)-layer case is much more difficult to optimize in fabrication due to the more sub-layers. The theoretical solution obtained above can be used to aid the electrode development by greatly reducing the number of trials required. Note that though numerical methods are also required to plot the explicit solutions, the numerical procedure is fundamentally different with those that directly solve implicit solutions or differential equations which may have numerical issues such as truncation errors or divergence. Further, as mentioned in the preceding section, the triple-layer case is used as a simple example to introduce the concept of the multi-layer configuration. Four or five-layer configurations can be developed for further elec-

trode optimization. Their solutions are much more complicated and longer in expression, therefore are excluded in this paper.

3. Results and discussion

Fig. 2 presents the electrolyte phase potential variation $\Phi^{(m)}(\bar{x}) - \Phi_{\delta}^{(m)}$ or the overpotential difference $\Delta\eta$ (left column) and normalized local transfer current density (right column) through the cathode electrode for general dual-layer configurations. To simplify the discussion, we set all the quantities in Layer 1 constant. The electrode properties are listed in Table 1. It can be seen that in

Layer 2 the electrolyte phase potentials and reaction currents are different when changing its properties. The trends are similar when changing one property for different thickness ratios. Note that a change in the ionic conductivity also leads to a shift in the profiles, which can be explained by the fact that the ionic conductivity will affect the electrolyte phase potential (see Eq. (1)) which impacts the reaction rate (see Eq. (2)). In addition, a thicker Layer 2 will enlarge the impact of the other properties. Note that changing the ionic conductivity in Layer 2 leads to a continuous transition from Layer 1 to 2, while the case of the effective exchange current indicates a jump at the layer interface in the curves of reaction current. This was explained in our previous paper [4] in detail.

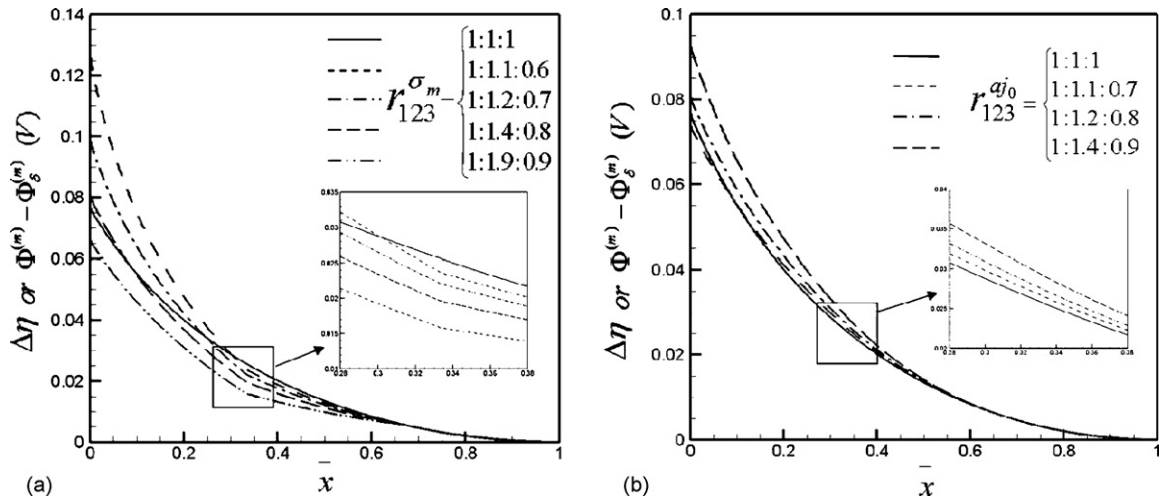


Fig. 3. Profiles of $\Delta\eta$ or $\Phi^{(m)}(\bar{x}) - \Phi_{\delta}^{(m)}$ in the electrode with varying $r_{123}^{\sigma m}$ s (a) and $r_{123}^{aj_0}$ s (b) when $\Delta U^{j_s} = 0.1$ V.

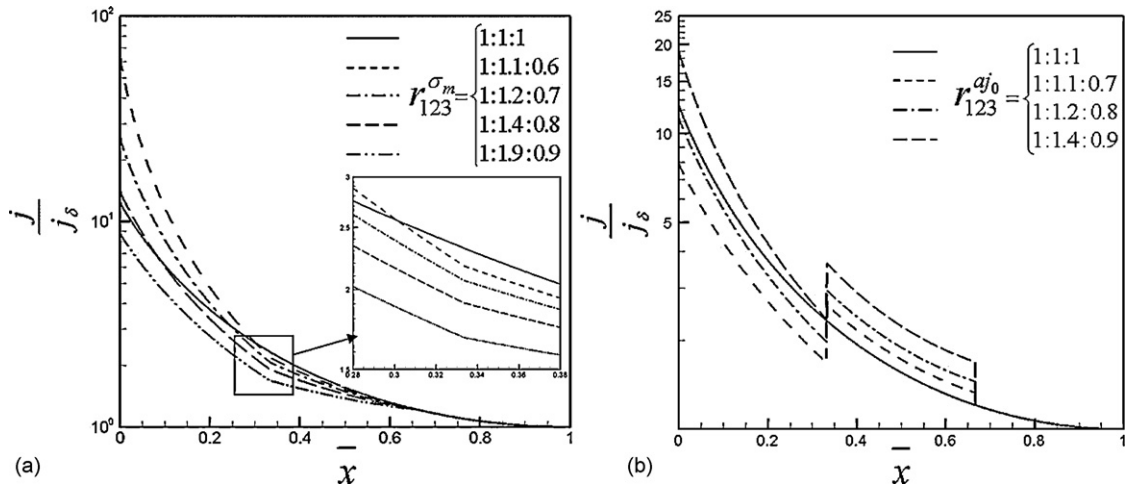


Fig. 4. Profiles of the dimensionless transfer current densities j/j_{δ} with varying $r_{123}^{\sigma m}$ s (a) and $r_{123}^{aj_0}$ s (b) when $\Delta U^{j_s} = 0.1$ V.

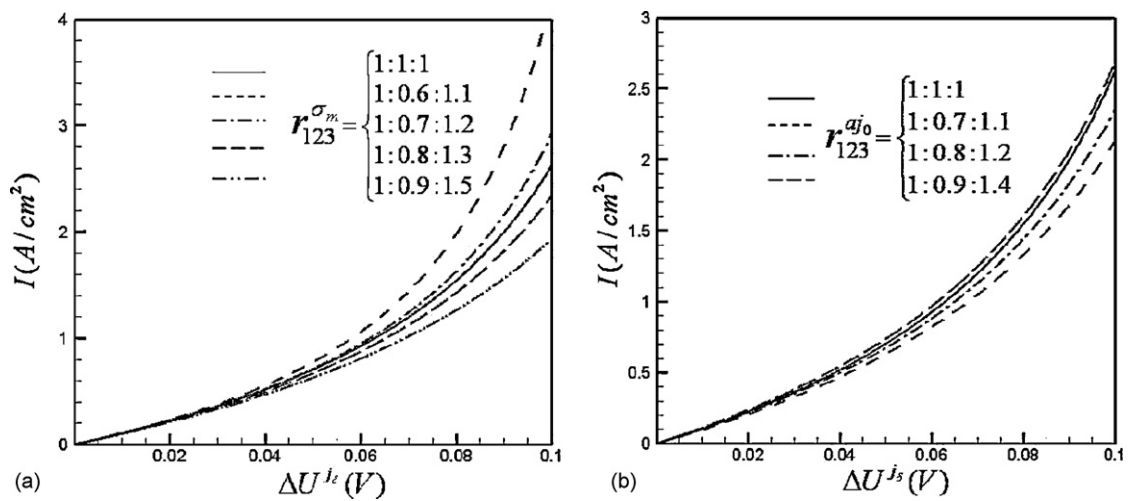


Fig. 5. Profiles of the average current densities I with varying $r_{123}^{\sigma m}$ s (a) and $r_{123}^{aj_0}$ s (b).

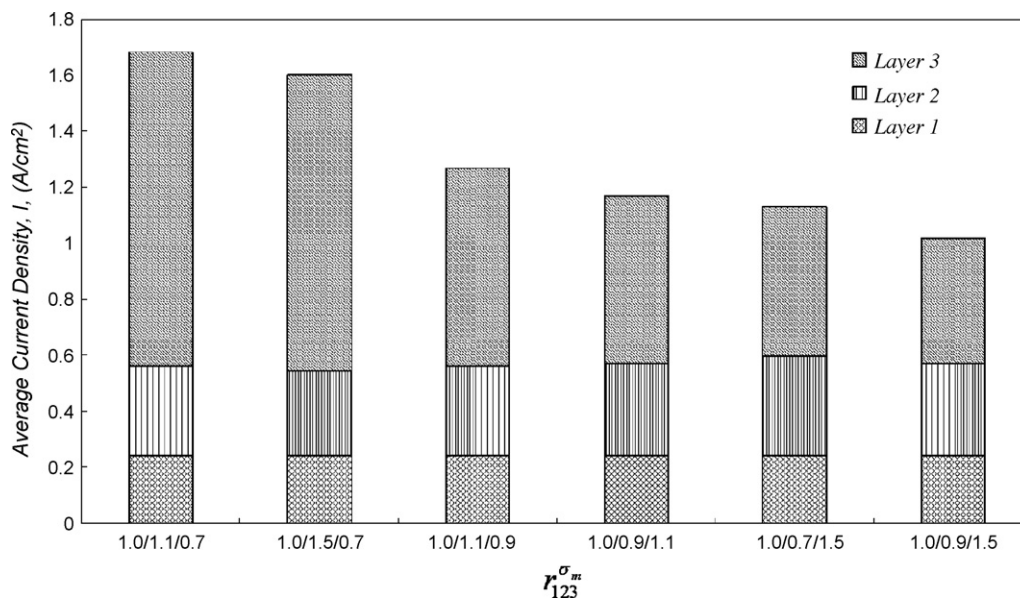


Fig. 6. The average current density in each layer with varying $r_{123}^{\sigma_m}$ s when $\Delta U^j_s = 0.07$ V.

Fig. 3 presents for the triple-layer configuration the distribution of the electrolyte phase potential variation with different $r_{123}^{\sigma_m}$ (left) and $r_{123}^{a_0}$ (right) at ΔU^j_s of 0.1 V. Note we define $r_{123}^{\sigma_m} = (\sigma_m^{eff})_1 : (\sigma_m^{eff})_2 : (\sigma_m^{eff})_3$ and $r_{123}^{a_0} = (a_{0,T}^{c,ref})_1 : (a_{0,T}^{c,ref})_2 : (a_{0,T}^{c,ref})_3$. The electrode consists of three sub-layers with the same thickness, and again the physical properties of Layer 1 are set constant. The solid lines always denote results of the single-layer case, in which the physical properties are uniform through the whole domain. It can be seen that when the ionic conductivity in Layer 2 is greater than that of Layer 1, the slope decreases in Layer 2. An increasing ionic conductivity in Layer 3 also reduces the variation in the overpotential change in Layer 3. A transition point is evi-

dent at the Layers 2–3 interface when considering different layer ionic conductivities. The transition is not obvious at the interface when changing the effective exchange current, as shown in Fig. 3(b).

Fig. 4 shows the profiles of the corresponding local transfer current density. Similar trends to the previous figure are indicated for different layer ionic conductivities, while Fig. 4(b) shows a quite different shape comparing with Fig. 3(b). The sub-layer boundaries are clearly indicated by the jumps in the reaction current profile in Fig. 4(b), which is similar to Fig. 2 (left). Fig. 5 shows the overall average current density at varying properties of Layers 2 and 3. It can be seen that the impacts of their properties are evident at high ΔU^j_s .

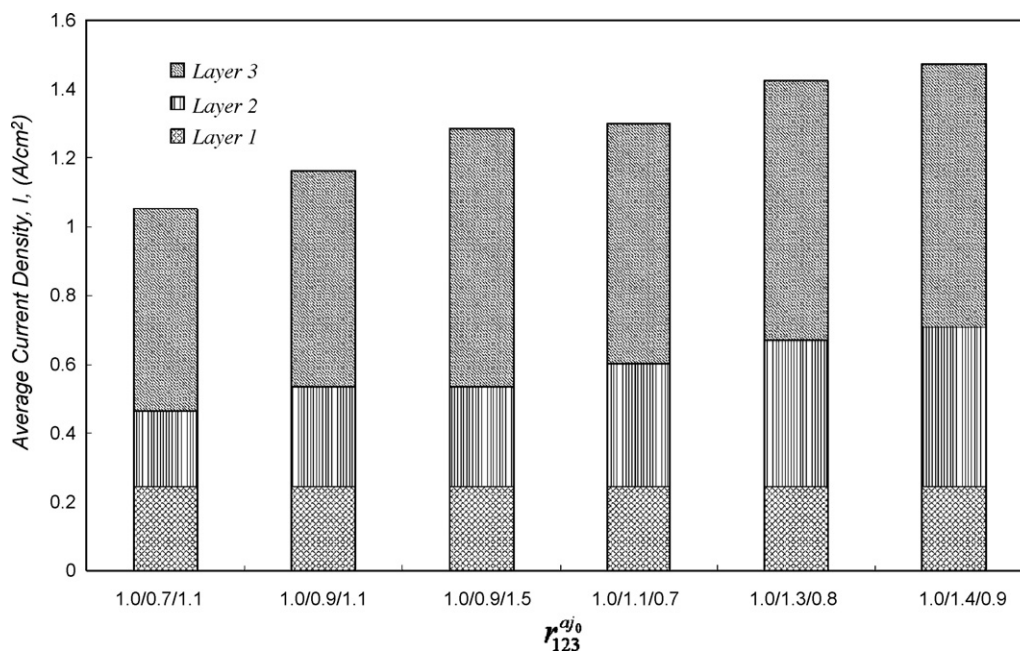


Fig. 7. Stacked columns of average current density I in each layer with varying $r_{123}^{a_0}$ s when $\Delta U^j_s = 0.07$ V.

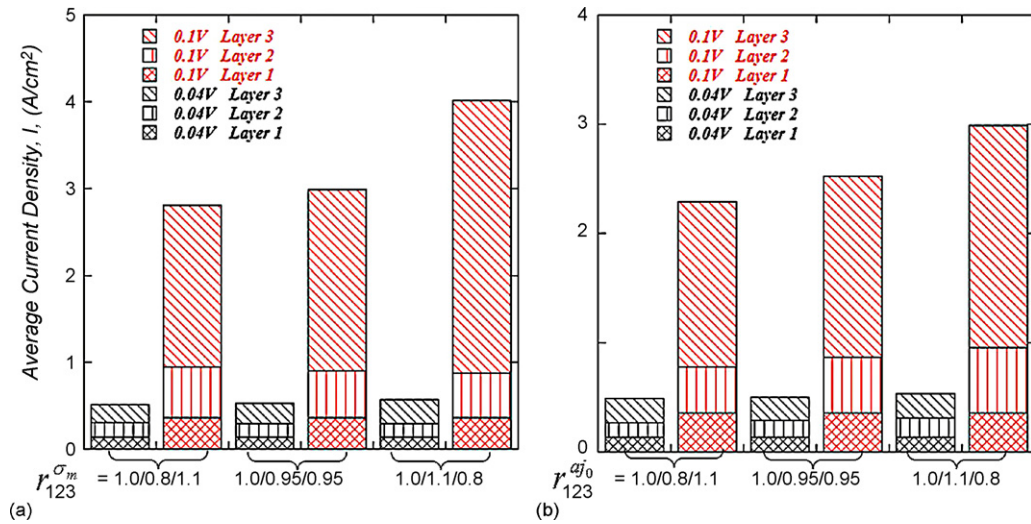


Fig. 8. Comparison of the average current densities at varying $r_{123}^{\sigma_m}$ s (a) and $r_{123}^{a_{j_0}^{c,ref}}$ s (b) for two $\Delta U^{j,\delta}$ s: one is 0.04 V, the other 0.1 V.

In order to further discuss the contribution of each layer especially the one adjacent to the membrane, Fig. 6 presents the average current density in each layer with an increasing ionic conductivity for Layer 3. It is evident from this figure that Layer 3 contributes a major portion of current production. It is again observed that a higher ionic conductivity σ_m^{eff} (comparing with that of Layer 1) leads to a relatively lower average current in Layer 3. Additionally, this figure depicts that the Layer 3 performance is also dependent on the physical properties of Layer 2: though the ionic conductivity ratio of Layers 1 and 3 are the same for the first two columns, changing the Layer 2 property also induces an observable distinction on the current of Layer 3. Similar phenomenon can be observed in the last two columns (1.0/0.7/1.5 and 1.0/0.9/1.5).

Fig. 7 presents the impact of the effective transfer current $a_{j_0,T}^{c,ref}$ on the average current density in each sub-layer. It can be seen that the average current increases with the effective transfer current in each layer. However, the change in the former is not proportional to the one of the latter, which is primarily due to the interaction among sub-layers. For an instance, from Columns 3 to 4 the Layer 3's $a_{j_0,T}^{c,ref}$ is reduced by more than half, while the current of Layer 3 in the latter case is still more than half of the one in Column 3. In addition, if Layers 2 and 3 are treated as one combined layer, in Column 1 and 4 this combined layer has the same Pt loading (if $a_{j_0,T}^{c,ref}$ is proportional to the Pt loading). However, the two columns indicate different performances, which demonstrates that distribution of the Pt loading also affects the electrode performance. Further, Layer 3 shows a higher Pt utilization. For an example in the fourth case, though $a_{j_0,T}^{c,ref}$ of Layer 3 is less than 70% of that in other layers, its current is still over the one in the others.

Fig. 8 compares the sub-layer performance at different $\Delta U^{j,\delta}$ s. The average values in Layers 2 and 3 are 0.95 for all the considered case, i.e. the overall loading amount of a material (either the ionomer or Pt) is the same for all the cases in these two sub-layers. However, the columns exhibit distinct performances at high $\Delta U^{j,\delta}$ s when material loadings are allocated differently in these two sub-layers. The implication of this result is that in a dual-layer electrode one sub-layer can be further optimized using multi-layer configuration, i.e. the more sub-layers, the better way we can optimize the electrode performance. Detailed discussion on the parameter of $\Delta U^{j,\delta}$ can be found in our previous studies on the single-layer electrode [3]. It can be seen that at high $\Delta U^{j,\delta}$ s both $a_{j_0,T}^{c,ref}$ and σ_m^{eff} in Layer 3 have profound effects on the current production in this layer as well as the overall current density, while the properties in

Layer 2 have a relatively small influence. However, the impacts are not remarkable at low $\Delta U^{j,\delta}$ s.

4. Conclusions

THIS paper investigated a dual-layer electrode configuration with different layer thicknesses and a triple-layer one for PEFCs. Explicit solutions were obtained for the profiles of the electrolyte phase potential and exchange current density in both cases. These important quantities in the electrode, together with the average current within each layer and overall current, were plotted at varying ratios of the sub-layer thickness, ionic conductivity (relevant to the electrolyte ionomer loading), and effective transfer current density. We found that changing these properties in each sub-layer alters the profiles of the phase potential and local current production across the electrode. For the triple-layer configuration, the properties in the layer adjacent to the electrolyte membrane indicate a profound influence on the local reaction and overall current production. Results also indicated that though the average properties (or material loadings) over Layers 2 and 3 are the same, the overall performance of these two layers may be different and depends on the allocation of the material loadings in each layer. The impact of sub-layers' properties is found to highly depend on the lumped parameter $\Delta U^{j,\delta}$. At low $\Delta U^{j,\delta}$ s, their influence is not remarkable.

Acknowledgement

Partial support of this work by the SETsquared UK US Collaborative Program is gratefully acknowledged.

Appendix A. Nomenclature

a	effective catalyst area per unit volume or specific area, m^2/m^3
C	molar concentration, mol/m^3
D	species diffusivity, m^2/s
F	Faraday's constant, 96,487 C/equiv.
I	average current density, A/cm^2
j	transfer current density, A/cm^2
k	thermal conductivity, $\text{W}/\text{m K}$
P	pressure, Pa

where

$$\begin{aligned} \Psi^{\text{II}} &= \Pi \left(\Delta U^{\text{II}}, \frac{2}{3} \right) (1 - r_{12}^{\sigma m} \cdot r_{12}^{\text{aj}0}) + 1, \\ \Psi^{\text{III}} &= \Psi^{\text{II}} \Pi^{\text{II}} \left(\Delta U^{\text{II}}, \frac{1}{3} \right) (1 - r_{23}^{\sigma m} \cdot r_{23}^{\text{aj}0}) + \Psi^{\text{II}} + \\ & r_{23}^{\sigma m} \cdot r_{23}^{\text{aj}0} \cdot \Psi^{\text{II}} \Pi^{\text{II}} \left(\Delta U^{\text{II}}, \frac{2}{3} \right) - r_{13}^{\sigma m} \cdot r_{13}^{\text{aj}0} \cdot \Pi \left(\Delta U^{\text{II}}, \frac{2}{3} \right), \\ \Pi^{\text{II}} &= \left[\tan \left(\sqrt{\frac{\alpha_c F \Delta U^{\text{II}}}{2 R_g T} \frac{r_{12}^{\sigma m}}{r_{12}^{\text{aj}0}} \Psi^{\text{II}}(\Delta U^{\text{II}}, r_{12}^{\sigma m}, r_{12}^{\text{aj}0})} \cdot \left(\bar{x} - \frac{2}{3} \right)} - \tan^{-1} \sqrt{\frac{\Pi \left(\Delta U^{\text{II}}, \frac{2}{3} \right)}{\Psi^{\text{II}}(\Delta U^{\text{II}}, r_{12}^{\sigma m}, r_{12}^{\text{aj}0})} r_{12}^{\sigma m} \cdot r_{12}^{\text{aj}0}} \right) \right]^2, \\ \Pi^{\text{III}} &= \left[\tan \left(\sqrt{\frac{\alpha_c F \Delta U^{\text{II}}}{2 R_g T} \frac{r_{13}^{\sigma m}}{r_{13}^{\text{aj}0}} \Psi^{\text{III}}(\Delta U^{\text{II}}, r_{13}^{\sigma m}, r_{23}^{\sigma m}, r_{13}^{\text{aj}0}, r_{23}^{\text{aj}0})} \cdot \left(\bar{x} - \frac{1}{3} \right)} - \tan^{-1} \sqrt{\frac{\Pi^{\text{II}} \left(\Delta U^{\text{II}}, \frac{1}{3} \right) - \Pi \left(\Delta U^{\text{II}}, \frac{2}{3} \right)}{\Psi^{\text{III}}(\Delta U^{\text{II}}, r_{13}^{\sigma m}, r_{23}^{\sigma m}, r_{13}^{\text{aj}0}, r_{23}^{\text{aj}0})} r_{23}^{\sigma m} \cdot r_{23}^{\text{aj}0}} + \frac{\Pi \left(\Delta U^{\text{II}}, \frac{2}{3} \right)}{\Psi^{\text{III}}(\Delta U^{\text{II}}, r_{13}^{\sigma m}, r_{23}^{\sigma m}, r_{13}^{\text{aj}0}, r_{23}^{\text{aj}0})} r_{13}^{\sigma m} \cdot r_{13}^{\text{aj}0}} \right) \right]^2 \end{aligned} \quad (15)$$

Note the ratio of the sub-layer thicknesses is not shown as a variable in the solution, instead we use the number 1/3 and 2/3 (i.e. the ratios) directly in the expression.

r	ratio of parameters
R	Ohmic resistance, $\text{m}\Omega \text{ cm}^2$
R_g	universal gas constant, 8.134 J/mol K
T	temperature, K
U_o	equilibrium potential, V

Greek symbols

α	transfer coefficient
Φ	phase potential, V
σ	conductivity, S/m
η	surface overpotential, V
δ	thickness, m

Superscripts and subscripts

c	cathode
eff	effective value
i	index of sub-layers
m	membrane phase
ref	reference value
s	solid

Appendix B. The explicit solution to the triple-layer electrode

Eqs. (1) and (10) can be analytically solved and the solution is as follows:

$$\begin{aligned} \Phi_1^{(m)} - \Phi_\delta^{(m)} &= \frac{R_g T}{\alpha_c F} \ln \{ \Pi(\Delta U^{\text{II}}, \bar{x}) + 1 \} \\ \Phi_2^{(m)} - \Phi_\delta^{(m)} &= \frac{R_g T}{\alpha_c F} \ln \left\{ \frac{\Psi^{\text{II}}(\Delta U^{\text{II}}, r_{12}^{\sigma m}, r_{12}^{\text{aj}0})}{[\Pi^{\text{II}}(\Delta U^{\text{II}}, r_{12}^{\sigma m}, r_{12}^{\text{aj}0}, \bar{x}) + 1]} \right\} \\ \Phi_3^{(m)} - \Phi_\delta^{(m)} &= \frac{R_g T}{\alpha_c F} \ln \left\{ \frac{\Psi^{\text{III}}(\Delta U^{\text{II}}, r_{13}^{\sigma m}, r_{23}^{\sigma m}, r_{13}^{\text{aj}0}, r_{23}^{\text{aj}0})}{[\Pi^{\text{III}}(\Delta U^{\text{II}}, r_{13}^{\sigma m}, r_{23}^{\sigma m}, r_{13}^{\text{aj}0}, r_{23}^{\text{aj}0}, \bar{x}) + 1]} \right\} \end{aligned} \quad (14)$$

References

- [1] C.Y. Wang, *Chem. Rev.* 104 (2004) 4727.
- [2] A.Z. Weber, J. Newman, *Chem. Rev.* 104 (2004) 4679.
- [3] Y. Wang, X.H. Feng, *J. Electrochem. Soc.* 155 (12) (2008) B1289.
- [4] Y. Wang, X.H. Feng, *J. Electrochem. Soc.* 156 (3) (2009) B403.
- [5] M. Eikerling, A.A. Kornyshev, *J. Electroanal. Chem.* 453 (1998) 89.
- [6] L. You, H. Liu, *Int. J. Hydrogen Energy* 26 (2001) 991.
- [7] C.C. Boyer, R.G. Anthony, A.J. Appleby, *J. Appl. Electrochem.* 30 (2000) 777.
- [8] E.A. Ticianelli, C.R. Derouin, S. Srinivasan, *J. Electroanal. Chem.* 251 (1988) 275.
- [9] Antoine, Y. Bultel, P. Ozil, *Electrochim. Acta* 45 (2000) 4493.
- [10] K.C. Neyerlin, W. Gu, J. Jorne, A. Clarke Jr., H.A. Gasteiger, *J. Electrochem. Soc.* 154 (2007) B279.
- [11] P.K. Das, X. Li, Z.S. Liu, *J. Electroanal. Chem.* 604 (2007) 72.
- [12] Y.-G. Yoon, T.-H. Yang, G.-G. Park, W.-Y. Lee, C.-S. Kim, *J. Power Sources* 118 (2003) 189.
- [13] Q. Wang, D. Song, T. Navessin, S. Holdcroft, Z. Liu, *Electrochim. Acta* 50 (2004) 725.
- [14] P. Jain, L.T. Biegler, M.S. Jhon, *Electrochem. Solid-State Lett.* 11 (2008) B193.
- [15] W. Sun, B.A. Peppley, K. Karan, *Electrochim. Acta* 50 (2005) 3359.
- [16] M. Secanell, K. Karan, A. Suleman, N. Djilali, *Electrochim. Acta* 52 (2007) 6318.
- [17] G. Wang, P.P. Mukherjee, C. Wang, *Electrochim. Acta* 52 (2007) 6367.
- [18] D. Song, Q. Wang, Z. Liu, T. Navessin, S. Holdcroft, *Electrochim. Acta* 50 (2004) 731.
- [19] P.P. Mukherjee, C.Y. Wang, *J. Electrochem. Soc.* 154 (2007) B1121.
- [20] S.S. Kocha, in: W. Vielstich, H. Gasteiger, A. Lamm (Eds.), *Handbook of Fuel Cells: Fundamentals, Technology and Applications*, vol. 3, John Wiley & Sons, Ltd., 2003.
- [21] M.K. Debe, in: W. Vielstich, H. Gasteiger, A. Lamm (Eds.), *Handbook of Fuel Cells: Fundamentals, Technology and Applications*, vol. 3, John Wiley & Sons, Ltd., 2003.
- [22] E.A. Ticianelli, E.R. Gonzalez, in: W. Vielstich, H. Gasteiger, A. Lamm (Eds.), *Handbook of Fuel Cells: Fundamentals, Technology and Applications*, vol. 2, John Wiley & Sons, Ltd., 2003.
- [23] J. Zhang, *PEM Fuel Cell Electrocatalysts and Catalyst Layers Fundamentals and Applications*, Springer, 2008.